An Integrated CMOS Micromechanical Resonator High-Q Oscillator

Clark T.-C. Nguyen, *Member, IEEE,* and Roger T. Howe, *Fellow, IEEE*

***Abstract*— A completely monolithic high-Q oscillator, fabricated via a combined CMOS plus surface micromachining technology, is described, for which the oscillation frequency is controlled by a polysilicon micromechanical resonator with the intent of achieving high stability. The operation and performance of micromechanical resonators are modeled, with emphasis on circuit and noise modeling of multiport resonators. A series resonant oscillator design is discussed that utilizes a unique, gain-controllable transresistance sustaining amplifier. We show that in the absence of an automatic level control loop, the closed-loop, steady-state oscillation amplitude of this oscillator depends strongly upon the dc-bias voltage applied to the capacitively driven and sensed μresonator. Although the high-Q of the micromechanical resonator does contribute to improved oscillator stability, its limited power-handling ability outweighs the Q benefits and prevents this oscillator from achieving the high short-term stability normally expected of high-Q oscillators.**

***Index Terms*— Fabrication, microelectromechanical devices, microelectromechanical systems (MEMS), micromachining, micromechanical, nonlinear oscillators, oscillators, oscillator stability, phase noise, resonators.**

I. Introduction

CRYSTAL oscillators are widely used to generate precision frequency standards for complex integrated circuits. The majority of applications that use crystal oscillators—from timekeepers in simple wristwatches to local oscillators in complex communication links—specifically take advantage of the extremely stable frequencies they generate. This frequency stability results in large part from the high quality factor Q typical of the quartz crystals used. In particular, oscillator phase noise, which must be minimized in reference oscillators, is inversely proportional to the square of Q. For piezoelectrically transduced quartz, depending upon the cut and frequency of the crystal, Q's in the range of 10^4–10^6 are common [1]. Q values this large are required to meet phase noise standards in communications reference oscillators—typically, -130 dBc/Hz at 1 kHz offset from the carrier for a 10-MHz crystal oscillator reference.

Unfortunately, these values of tank Q are presently not achievable by conventional integrated circuit (IC) technologies, which can realize capacitors with Q's on the order of 10^4 but cannot provide passive or active inductors with comparable Q's. Excessive series resistance substrate losses and distributed parasitic capacitance greatly limit the Q of planar IC spiral inductors to less than about 20 in the ultrahigh-frequency range [2]–[4]. Nevertheless, the growing interest in compact, wireless communications continues to fuel interest in fully monolithic reference oscillator implementations, which include the high-Q tank element as well as sustaining electronics on-chip. Thus far, miniaturized resonator tank technologies, such as thin-film bulk acoustic mode, piezoelectric resonators (FBAR's) [5], [6], have shown the most promise in achieving single-chip tanks with Q's higher than 1000. The FBAR approach, however, awaits improvements in process and trimming technologies.

The rapid growth of micromachining technologies makes feasible another mechanical resonator-based approach to realizing integrated high-Q tanks. With Q's of over 80 000 [7] under vacuum, and center frequency temperature coefficients in the range of -10 ppm/°C (several times less with nulling techniques) [8], polycrystalline silicon micromechanical resonators (abbreviated "μresonators") can serve well as miniaturized substitutes for crystals in a variety of high-Q oscillator and filtering applications. Using a planar process technology that merges micromechanical resonators with conventional integrated circuits, a fully monolithic high-Q oscillator can be implemented.

In this paper, we describe the design, fabrication, and performance of a fully monolithic high-Q oscillator utilizing a surface-micromachined polycrystalline silicon mechanical resonator modularly integrated with sustaining CMOS electronics [9], [10]. Section II begins with modeling and a general discussion of μmechanical resonators as signal-processing devices, including a circuit-perspective treatment of noise in mechanical resonators. Section III then addresses the design of high-Q oscillators referenced to such μresonators. Last, fabrication and experimental verification are covered in Sections IV and V.

II. Micromechanical Resonators

To simplify the task of integrating CMOS with micromechanics, capacitive excitation and detection is utilized for the μresonators in this work. A variety of capacitive transducer topologies are available in this technology, including parallel-plate [11] and interdigitated-comb [12] types. As will be explained, comb transducers offer better supply-voltage insensitivity, and are therefore used in this design.

Manuscript received May 4, 1998; revised September 30, 1998. This work was supported by the Berkeley Sensor & Actuator Center and by the Defense Advanced Research Project Agency under Cooperative Agreement F30602-97-2-0101.

C. T.-C. Nguyen is with the University of Michigan, Ann Arbor, MI 48109-2122 USA (e-mail: ctnguyen@eecs.umich.edu).

R. T. Howe is with the University of California, Berkeley, CA 94720 USA (e-mail: howe@eecs.berkeley.edu).

Publisher Item Identifier S 0018-9200(99)02439-7.

0018–9200/99$10.00 © 1999 IEEE

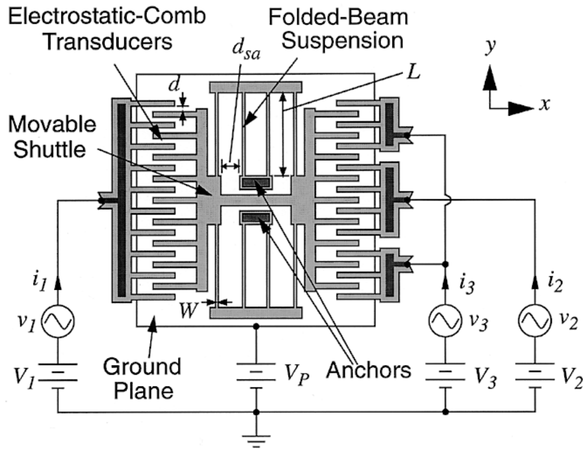

Fig. 1. Overhead view schematic of a three-port, comb-transduced μmechanical resonator under a general bias and excitation configuration. All areas of the resonator and electrodes are suspended 2 μm above the substrate, except for the darkly shaded areas, which are the anchor points.

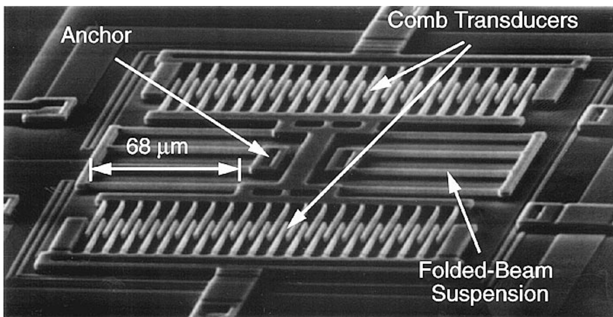

Fig. 2. SEM of a 100-kHz folded-beam, capacitive-comb transduced μresonator.

Fig. 1 shows the overhead view schematic of a three-port, capacitive-comb transduced μresonator, such as used for this work, in a general bias and excitation configuration [7], [12]. This μresonator consists of a finger-supporting shuttle mass suspended 2 μm above the substrate by folded flexures, which are anchored to a ground plane on the substrate at two central points. The shuttle mass is free to move in the x-direction, parallel to the plane of the silicon substrate. Folding the suspending beams as shown provides two main advantages: first, postfabrication residual stress is relieved if all beams expand or contract by the same amount; and second, spring stiffening nonlinearity in the suspension is reduced [13], since the folding truss is free to move in a direction perpendicular to the resonator motion (i.e., in the y-direction). The ground plane in electrical contact with the suspended, movable structure is essential to prevent pull-in of this structure [14], which for the 16.5-kHz μresonator of this work can occur for structure-to-substrate voltage differences as small as 4 V. In addition, symmetrical splitting of port 3, as shown, is necessary for predictable operation. A scanning-electron micrograph (SEM) of a 100-kHz version of this μresonator is presented in Fig. 2.

The fundamental resonance frequency of this mechanical resonator is determined largely by material properties and by geometry, and is given by the expression [12], [15]

TABLE I
μMECHANICAL RESONATOR DATA

Parameter	Value	Units
Folded-Beam Length, L	185.3	µm
Folded-Beam Width, W	1.9	µm
Structural Layer Thickness, h	2	µm
Static Shuttle-to-Anchor Gap, d_{sa}	16	µm
Effective Mass, m_r	5.73×10^{-11}	kg
System Spring Constant, k_r	0.65	N/m
No. Finger Overlaps at Port 1, N_{g1}	60	—
No. Finger Overlaps at Port 2, N_{g2}	30	—
No. Finger Overlaps at Port 3, N_{g3}	30	—
Finger Gap Spacing, d	2	µm
Finger Overlap, L_d	20	µm
$\partial C/\partial x$ per Finger Overlap	9.74×10^{-12}	F/m
Measured Q at 20 mTorr	23,400	—
Young's Modulus, E [12]	150	GPa
Density of Polysilicon, ρ	2300	kg/m
Calculated Resonance Frequency, f_o	16.9	kHz
Measured Resonance Frequency, f_o	16.5	kHz

$$f_0 = \frac{1}{2\pi}\left[\frac{2Eh(W/L)^3}{\left(M_P + \frac{1}{4}M_t + \frac{12}{35}M_b\right)}\right]^{1/2} \tag{1}$$

where M_P is the shuttle mass, M_t is the total combined mass of the folding trusses, M_b is the total combined mass of the suspending beams, W and h are the cross-sectional width and thickness, respectively, of the suspending beams, and L is indicated in Fig. 1. The dimensions and performance data for the prototype μresonator used in this work are summarized in Table I.

To bias and excite the device, a dc-bias voltage V_P is applied to the resonator and its underlying ground plane, while ac excitation voltages v_n are applied to the electrodes. For cases where $V_P \gg v_n$, the force exerted on the resonator by the excitation voltage at port n is dominated by

$$f_{dn} = \frac{1}{2}(V_{\text{P}n} - v_n)^2\frac{\partial C_n}{\partial x} \approx -V_{\text{P}n}\frac{\partial C_n}{\partial x}v_n \tag{2}$$

where x is the shuttle displacement, $\partial C_n/\partial x$ is the change in capacitance per unit displacement at port n, and $V_{\text{P}n} = V_P - V_n$. [In actual usage, the negative sign in (2) cancels with the sign of $\partial C_1/\partial x$ *at port 1*.] When an ac excitation with frequency close to the fundamental resonance frequency of the μresonator is applied, the μmechanical resonator begins to vibrate, creating a time-varying capacitance between the μresonator and the electrodes. Since the dc bias $V_{\text{P}n}$ is effectively applied across the time-varying capacitance at port n, a motional output current arises at this port, given by

$$i_{\text{x}n} = -V_{\text{P}n}\frac{\partial C_n}{\partial t} = -V_{\text{P}n}\frac{\partial C_n}{\partial x}\frac{\partial x}{\partial t}. \tag{3}$$

For this resonator design, the transducer capacitors consist of overlap capacitance between the interdigitated shuttle and electrode fingers. As the shuttle moves, these capacitors vary linearly (to first order) with displacement. Thus, $\partial C_n/\partial x$ is a constant, given approximately by the expression

$$\frac{\partial C_n}{\partial x} \approx \begin{cases} -\dfrac{\xi N_{\text{gn}}\,\epsilon_0 h}{d} & \text{(left-hand side)} \\ \dfrac{\xi N_{\text{gn}}\,\epsilon_0 h}{d} & \text{(right-hand side)} \end{cases} \tag{4}$$

where h is the shuttle finger thickness, d is the gap between electrode and resonator fingers (assumed constant for all finger pairings), and N_{gn} is the number of finger gaps at port n. ξ is a constant that models additional capacitance due to fringing electric fields. For the comb geometries used here (2-μm gaps, 2-μm-wide fingers, offset 2 μm above the ground plane), $\xi = 1.1$ [16]. Note from (4) that $\partial C_n/\partial x$ is inversely proportional to the gap distance.

For the 16.5-kHz μresonator design of this work, typical amplitudes of vibration are in the 0–16-μm range, and typical output currents are from 0 to 40 nA, with dc biases in the tens of volts and ac excitation amplitudes in the millivolt to tens of millivolts range. Amplitudes and currents will vary depending upon the overall stiffness of the resonator, which is a strong function of the folded-beam suspension length L.

A. Small-Signal Equivalent Circuit

With all other ports ac grounded, the effective impedance seen looking into a given port of a μmechanical resonator may be modeled by the parallel combination of a static capacitor representing the electrode-to-resonator (and electrode-to-ground plane) capacitance present when the resonator is motionless, and a motional admittance, modeling the circuit behavior when the resonator vibrates. The static capacitor is largely overlap capacitance and may be obtained via approximate analysis, or more exactly through finite element simulation. The motional admittance at a given port n is defined, in phasor form, as

$$Y_{\text{xn}}(j\omega) = \frac{I_{\text{xn}}(j\omega)}{V_n(j\omega)}. \tag{5}$$

Using the phasor form of (3), (5) may be expanded as

$$Y_{\text{xn}}(j\omega) = -j\omega V_{\text{Pn}} \frac{\partial C_n}{\partial x} \frac{X(j\omega)}{F_{\text{dn}}(j\omega)} \frac{F_{\text{dn}}(j\omega)}{V_n(j\omega)} \tag{6}$$

where $F_{\text{dn}}(j\omega)$ is the phasor drive force imposed by v_n. From (2), the phasor input voltage-to-drive force transfer function at port n is

$$\frac{F_{\text{dn}}(j\omega)}{V_n(j\omega)} = -V_{\text{Pn}} \frac{\partial C_n}{\partial x}. \tag{7}$$

The drive force-to-displacement transfer function is given by [17]

$$\frac{X(j\omega)}{F_{\text{dn}}(j\omega)} = \frac{k_r^{-1}}{1 - (\omega/\omega_o)^2 + j(\omega/Q\omega_o)} \tag{8}$$

where ω_o is the natural (radian) resonance frequency, k_r is the system spring constant, and Q is the quality factor of the resonator system. Using (7) and (8) in (6), we have for motional impedance at port n (with all other ports grounded)

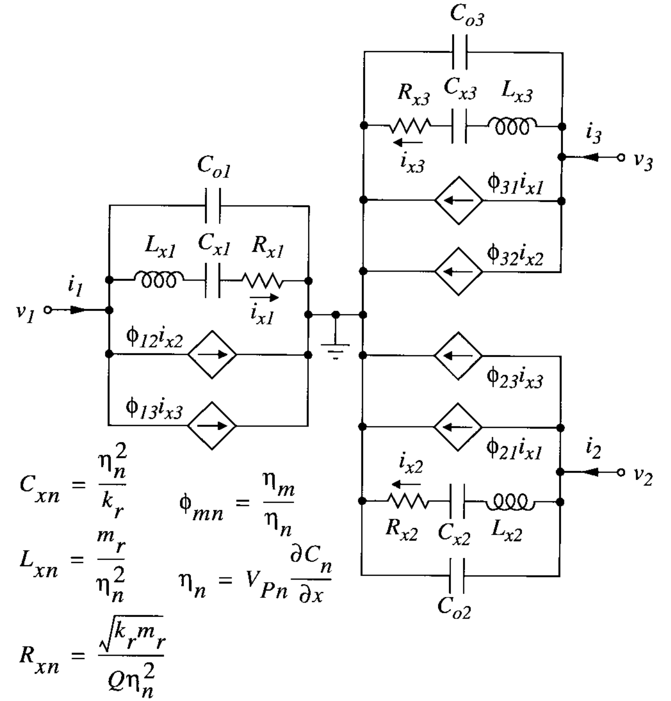

Fig. 3. Small-signal equivalent circuit for a three-port μmechanical resonator with equations for the elements. In the equations, m_r is the effective mass of the resonator, k_r is the system spring constant, and $\partial C_n/\partial x$ is the change in capacitance per unit displacement at port n.

$$Y_{\text{xn}}(j\omega) = \frac{j\omega k_r^{-1} V_{\text{Pn}}^2 \left(\dfrac{\partial C_n}{\partial x}\right)^2}{1 - (\omega/\omega_o)^2 + j(\omega/Q\omega_o)}. \tag{9}$$

Equation (9) has the form of a bandpass biquad, and thus may be modeled by a series inductor-capacitor-resistor *(LCR)* circuit.

The above derivation was performed for the case of one port with all other ports tied to ac ground. For the general case where all ports receive ac signals, each port influences the total resonator displacement. Thus, the current arising at each port is determined by the input not only at that port but also at all other ports. To model this port-to-port coupling, current-controlled-current sources (CCCS's) may be used [11], [18]. The small-signal equivalent circuit modeling the three-port capacitively transduced μmechanical resonator of this work then takes the form shown in Fig. 3, where each port is modeled by a static capacitor in parallel with a series *LCR* and CCCS's coupling the given port with all others. Equations for the elements are also given in Fig. 3. The element values for the 16.5-kHz μresonator of this work are summarized in Table II for $V_{\text{Pn}} = 35$ V. Within a range of sufficiently small drive voltages, these values match extracted values obtained through characterization techniques described in Section V.

Depending upon the type of application, parasitic capacitors coupling the ports can also be added to the circuit of Fig. 3.

TABLE II
μRESONATOR EQUIVALENT CIRCUIT ELEMENT VALUES

Element	Port 1 (n=1)	Port 2 (n=2)	Port 3 (n=3)	Units
C_{on}	11.7	5.8	5.8	fF
C_{xn}	0.65	0.16	0.16	fF
L_{xn}	136.5	545.8	545.8	kH
R_{xn}	620.8	2483.1	2483.1	kΩ
ϕ_{mn}	$\phi_{12} = -2$	$\phi_{21} = -0.5$	$\phi_{31} = -0.5$	A/A
	$\phi_{13} = -2$	$\phi_{23} = 1$	$\phi_{32} = 1$	A/A

* Calculated using values in Table I and V_{Pn}=35V.

Such capacitors are negligible for the low-frequency, high-Q application of this work but are essential for accurate modeling of higher frequency applications, or for off-chip implementations where bond wires and large bond pads are used [18].

B. Supply Sensitivity of Frequency

The dependence of resonance frequency on dc bias V_{Pn} for the comb-transduced resonator of this work is best evaluated via comparison with parallel-plate capacitively transduced resonators. As is well documented, the resonance frequency of the latter is controllable by adjusting the dc-bias voltage applied across any resonator-to-electrode parallel-plate capacitor gap [14], [18]. This voltage dependence of the resonance frequency arises due to the nonlinear dependence of resonator-to-electrode capacitance on resonator displacement x for parallel-plate gaps. Effectively, this nonlinearity generates an electrical spring constant k_{en} that varies with V_{Pn} and that subtracts from the mechanical spring constant of the resonator, lowering its resonance frequency [18].

Although useful for voltage-controlled oscillators, this feature is not desirable in a reference oscillator, since it adds a component of frequency instability with respect to variations in power supply. The use of capacitive-comb transduction in this work eliminates this component of frequency instability to first order by linearizing the x-dependence of the resonator-to-electrode capacitance, as explained in relation to (4). The electrical spring constant for this resonator, then, is nonexistent (to first order), and the resonator center frequency is independent of V_{Pn}.

For actual comb-driven μresonators, nonidealities, such as levitation [20] and end effects [13], do not permit absolute cancellation of k_{en}, and some variation of frequency with V_{Pn} is observed. Fig. 4 shows a plot of center frequency versus dc bias for a micromachined comb-driven resonator measured in vacuum under small-amplitude, linear conditions. The frequency variation is about -54 ppm/V at $V_P = 15$ V and increases as V_P increases. If $V_P = 15$ V is supplied by a Zener diode reference, which typically varies 388 mV over a $-55°$ to 100°C range [21], the corresponding fractional frequency variation for this μresonator is 21 ppm over this temperature range. If a bandgap reference is used (2 mV variation over a $-55°$ to 100°C range [21]), the $\Delta f/f_o$ variation is 0.1 ppm. Both of the above are acceptable for most reference oscillator applications, although use of the bandgap reference version will probably be preferred for more stringent cellular communications applications.

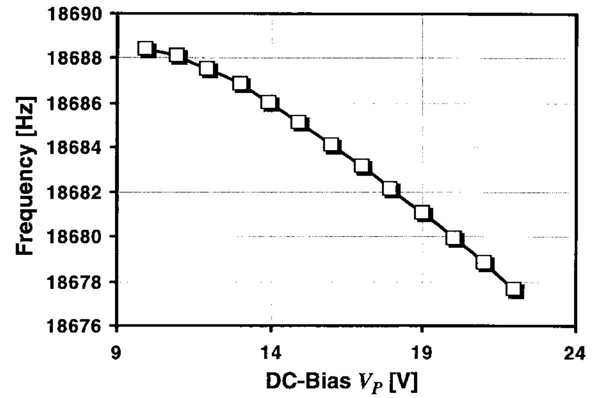

Fig. 4. Plot of center frequency versus dc-bias voltage V_P for a comb-driven μresonator.

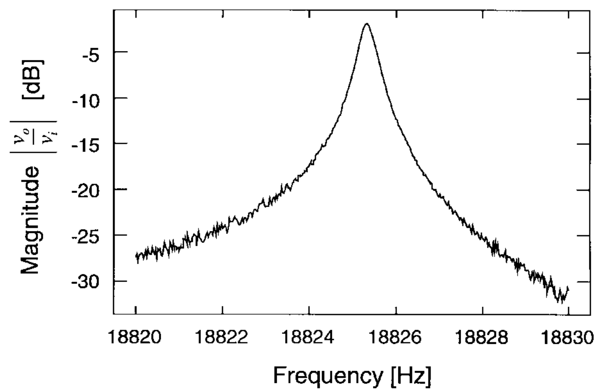

Fig. 5. Measured transconductance spectrum for a folded-beam, capacitive-comb transduced polysilicon μmechanical resonator operated under a vacuum pressure of 20 mtorr.

C. Quality Factor

To attain high Q, μmechanical resonators should be operated in vacuum to eliminate losses due to fluidic damping mechanisms [22]–[24]. For μmechanical resonators with Q's in the range of 50 000 to 500 000, viscous gas damping ceases to be the dominant energy-dissipation mechanism at pressures in the range of 0.1–1 mtorr [23], where intrinsic material damping mechanisms become dominant [25], [26], and the Q of the μresonator is maximized.

Fig. 5 presents the transconductance spectrum for a folded-beam, capacitive-comb transduced polysilicon μmechanical resonator measured under a vacuum pressure of 20 mtorr, with $V_P = 20$ V and $v_i = 1$ mV peak (small-amplitude, linear conditions). The measurement apparatus will be detailed in Section V. The spectrum in Fig. 5 is extremely selective, with a quality factor Q of 51 000. For lower pressures, the Q is even larger, exceeding 80 000. This demonstrated degree of frequency selectivity makes μmechanical resonators well suited to high-Q oscillator applications.

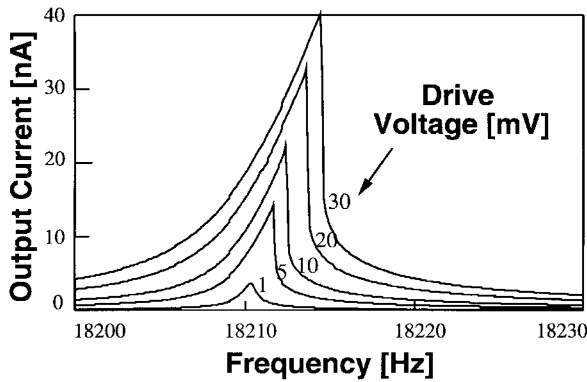

Fig. 6. Output current versus frequency for varying drive-voltage amplitudes for a folded-beam, comb-driven μmechanical resonator measured under 20-mtorr vacuum with $V_P = 30$ V and with frequency swept downward (sweep time = 10 min).

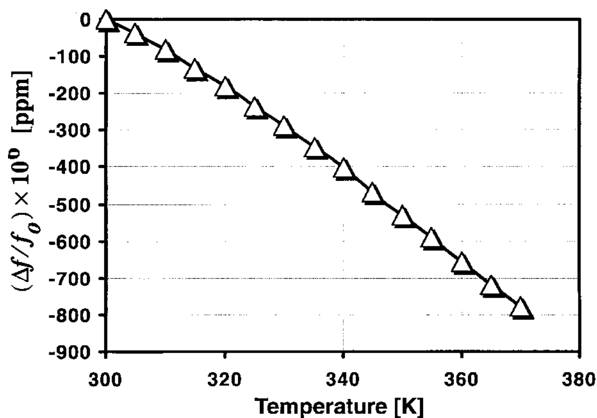

Fig. 7. Measured plot of fractional frequency change $\Delta f/f$ versus temperature for a folded-beam, capacitive-comb transduced polysilicon μmechanical resonator. (Frequency measurements were made under small-amplitude, linear conditions for this plot—i.e., $V_P = 20$ V and $v_i = 1$ mV.)

D. Nonlinearity

Although the use of comb-capacitive transduction and folded beams greatly linearizes the resonator transconductance characteristic over comparable clamped–clamped, parallel-plate driven resonators, some nonlinearity is still visible under increasing drive voltages. This is illustrated in Fig. 6, which plots resonator output current versus frequency for a range of drive voltage amplitudes. The jump phenomena and shift in peak currents seen at higher drive voltages in Fig. 6 are a direct result of an odd-ordered nonlinearity in the μresonator's equation of motion, often called Duffing distortion [27]. For the case of capacitively transduced μresonators, this nonlinearity is caused by a combination of mechanical spring stiffening and effective electrical spring (k_e) softening [18].

E. Thermal Stability

The use of a tank element with large quality factor helps to insure excellent short-term frequency stability in oscillators. To insure exceptional long-term stability, the temperature coefficient of the resonance frequency and the aging rate of the tank element must be minuscule.

Fig. 7 shows a measured plot of fractional frequency change $\Delta f/f$ versus temperature for a folded-beam, capacitive-comb transduced polysilicon μmechanical resonator fabricated using the surface-micromachining process to be detailed in Section IV. Again, the measurement was performed under small-amplitude, linear conditions using the apparatus to be described in Section V. From the slope of the curve, the temperature coefficient of the resonance frequency TC_{fo} for this device is -10 ppm/°C. Through manipulation of (1), the temperature coefficient of the Young's modulus TC_E may be expressed as

$$TC_E = 2TC_{\text{fo}} - TC_h. \tag{10}$$

Using the measured value of $TC_{\text{fo}} = -10$ ppm/°C, (10) yields $TC_E = -22.5$ ppm/°C. This value is considerably smaller than a previously reported number of -74.5 ppm/°C [28], and it is stated tentatively pending a more systematic study of other factors that can affect the TC_{fo}.

The measured TC_{fo} of -10 ppm/°C can be reduced further via on-chip compensation or on-chip oven-control techniques. Such integrated oven control has been demonstrated that reduced the TC_{fo} of a capacitive-comb transduced μresonator to -2 ppm/°C [8], at the cost of a more complex micromachining process.

F. Thermal Noise

If the ambient temperature around a damped mechanical resonator is finite (i.e., not 0 K), and if the system is in thermal equilibrium, then the mechanical resonator must exhibit some degree of random (Brownian) motion. This random vibration constitutes thermal noise in the mechanical domain.

The magnitude of the random vibration is dependent upon the amount of damping in the oscillator system. To see this, consider that to avoid violating the second law of thermodynamics, the model for a *damped,* simple harmonic oscillator must include a noise force generator with sufficient amplitude to maintain the degree of random vibration dictated by the temperature of the system. Without this noise force generator, the damping of the system would force any oscillation to decay to zero, implying a system temperature of 0 K, which will violate thermal equilibrium requirements if the ambient temperature is not 0 K. Thus, the magnitude of the noise force generator should depend upon both temperature and the amount of damping in the system.

An expression for the noise force f_n can be obtained using the equipartition theorem [18], [29], [30], which states that any mode of a system in thermal equilibrium has an average noise energy of (1/2)kT, where k is Boltzmann's constant (1.38 $\times$ 10^{-23} J/K) and T is the temperature in kelvin. Through equilibrium arguments [30], the action of all modes (including molecular vibrations, velocity, etc.) may be combined into the action of an "ordered" mode, such as vibration of a mass-spring system. The average noise displacement of the mass in a mass-spring-damper oscillator system, assuming a dominant mode in the x-direction, is given by

$$\tfrac{1}{2}\, k_r \langle x_n^2 \rangle = \tfrac{1}{2}\, kT \tag{11}$$

where x_n is the displacement noise and $\langle x_n^2 \rangle$ is equal to the integral of $|x_n|^2$ over all frequencies. Inserting the expression for $|x_n|^2$ [from (8)], then integrating and rearranging, the expression for noise force density is found to be [30]

$$\frac{\overline{f_n^2}}{\Delta f} = \frac{4k_r kT}{\omega_o Q} = \frac{4\sqrt{k_r m_r}\, kT}{Q} \tag{12}$$

where Δf denotes a unit bandwidth. Note that this noise force is white over the thermal bandwidth. In converting from force to displacement, the noise is shaped by the force-to-displacement transfer function of the mechanical resonator, given by (8). Thus, the displacement noise $\overline{x_n^2}$ peaks at the resonance frequency (where oscillators operate). Note that this noise power is Q^2 times larger than that for mechanical devices operating below resonance, such as accelerometers [31]. From (12), an expression for noise displacement at resonance may be obtained as follows:

$$\frac{\overline{x_n^2}}{\Delta f} = \frac{Q^2}{k_r^2}\frac{\overline{f_n^2}}{\Delta f} = \frac{4Q\sqrt{m_r}kT}{k_r^{3/2}}. \tag{13}$$

Using (13) and the expression for output current as a function of displacement for a capacitively transduced resonator (3), the noise current at resonance is given by

$$\frac{\overline{i_n^2}}{\Delta f} = \omega_o^2 V_P^2 \left(\frac{\partial C}{\partial x}\right)^2 \frac{\overline{x_n^2}}{\Delta f} = \frac{4kT}{R_x} \tag{14}$$

where R_x is the series motional resistance of the microresonator seen at resonance at the port in question. Note that (14) is exactly the expression for thermal noise in a resistor with value R_x. Off resonance, this noise is shaped by the resonator frequency characteristic. Thus, the thermal noise performance of a micromechanical resonator is modeled completely by the noise performance of its equivalent circuit. When modeling noise in the equivalent circuit for three-port resonators, shown in Fig. 3, only one of the resistors should be given a noise source, since the current-controlled current sources will distribute this noise proportionately to the other ports. The other resistors should be considered noiseless. They are present only to model the distribution of power in the multiport resonator.

To minimize thermal voltage noise power in μresonators, this theory suggests that the series resistance R_x be minimized. From the equation for R_x in Fig. 3, this in turn requires that the electromechanical coupling factor η be maximized. η is largest when V_P and $\partial C/\partial x$ are maximized. Since $\partial C/\partial x$ is maximized when the electrode-to-resonator gaps are minimized, μresonator voltage noise performance improves as the electrode-to-resonator gap decreases. V_P is constrained by either the maximum voltage in a given system (obtained via the supply or via charge pumping) or electrostatic pull-in [11] of drive electrode and shuttle fingers, which shorts these fingers together and destroys the μresonator. For the devices of this work, which had 2-μm finger gaps, finger-to-finger pull-in occurred for V_P's greater than about 140 V.

III. Oscillator Design

As previously mentioned, the frequency stability of an oscillator is maximized when its Q is maximized. For this reason, oscillator architectures are often chosen to minimize the degradation of tank Q due to loading by sustaining circuitry. As a consequence, the choice of oscillator architecture is often determined by the size of the internal series resistance R_x of the tank element [34], since this dictates the size of the load resistance presented to the tank. In particular, in series resonant circuit topologies, a load resistance equal to or somewhat less than the tank's R_x is used, since this alleviates Q loading. Conversely, in parallel resonant circuit topologies, a load resistance much larger than that of the tank's R_x is often needed.

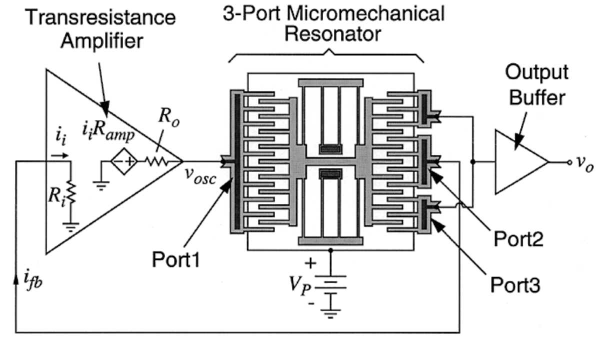

Fig. 8. System-level schematic for the μresonator oscillator.

As is evident from Table II, the R_x of the μresonator tank used here is rather large, typically exceeding 600 kΩ. A series resonant oscillator architecture was thus chosen in this work mainly to avoid the need for a very high impedance node in a parallel resonant circuit [34]. Fig. 8 shows a system-level schematic describing the basic series resonant architecture used for this oscillator. As shown, the system consists of a three-port μmechanical resonator, for which two ports are embedded in a (zero phase shift) positive feedback loop in series with a sustaining transresistance amplifier, while a third port is directed to an output buffer. The use of a third port effectively isolates the sustaining feedback loop from variations in output loading.

Assuming that the bandwidth of the sustaining transresistance amplifier is much larger than the oscillation frequency (so as to prevent excess phase shift at that frequency), oscillation will occur when the loop gain A_l is larger than unity. For this series resonant oscillator design, the loop gain is given by

$$A_l = \frac{R_{\text{amp}}}{R_{x12} + R_i + R_o} = \frac{R_{\text{amp}}}{R_{tot}} \tag{15}$$

where R_i is the small-signal input resistance of the transresistance amplifier, R_o is its output resistance, R_{amp} is its transresistance gain, and R_{x12} is the small-signal equivalent series motional resistance between ports 1 and 2 of the μmechanical resonator, defined by

$$R_{x12} = -\frac{v_1}{i_2} \tag{16}$$

where variables are defined in Fig. 3.

The value R_{x12} can be determined using Fig. 3. Driving this circuit at port 1 and grounding all other ports, we have (at resonance)

$$i_2 = \phi_{21} i_{x1} \quad \text{and} \quad i_{x1} = \frac{v_1}{R_{x1}}. \tag{17}$$

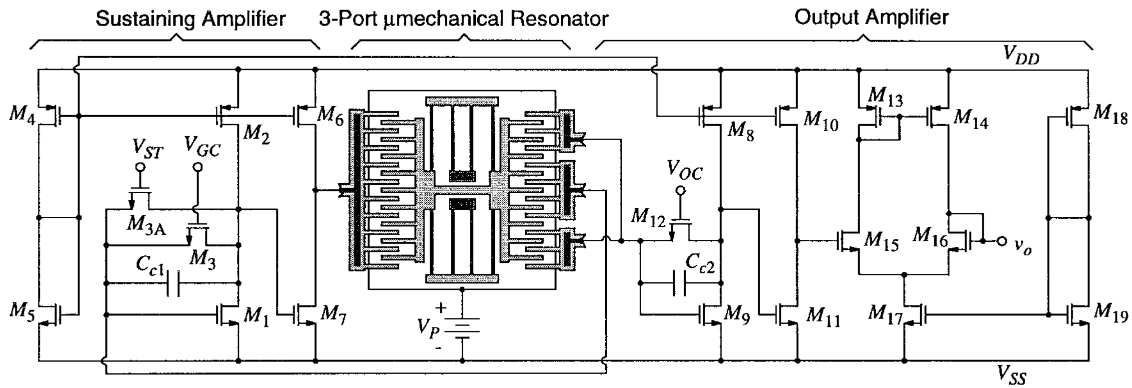

Fig. 9. Circuit schematic for the μresonator oscillator.

Applying (17) to (16), we have

$$R_{x12} = -\frac{R_{x1}}{\phi_{21}} = \frac{R_{x1}}{|\phi_{21}|}. \tag{18}$$

Using the data in Table II, we find $R_{x12} = 1.24$ MΩ for $V_P = 35$ V.

Conceptually, this oscillator may also be modeled as a high-Q negative resistance oscillator, with the quantities $(-R_{\text{amp}})$ and $(R_{x12} + R_i + R_o)$ comprising negative and positive resistances, respectively. During startup, if $A_l > 1$, the negative (trans)resistance of the amplifier R_{amp} is larger in magnitude than the positive resistance $(R_{x12} + R_i + R_o)$, and oscillation results. Oscillation builds up until either some form of nonlinearity or a designed automatic-level control circuit alters either or both resistors so that

$$R_{\text{amp}} = R_{x12} + R_i + R_o \tag{19}$$

at which point $A_l = 1$ and the oscillation amplitude limits. Under conditions where the amplitude of oscillation is large enough to cause nonlinearity in a given oscillator component, the associated resistance parameter (e.g., R_{x12} if the nonlinearity arises from the μmechanical resonator, R_{amp} if it comes from the amplifier) in (19) can be represented by a "large signal" equivalent, obtained through consideration of only fundamental components, neglecting higher order distortion harmonics [35], [36]. This holds because, as is the case with other high-Q oscillators (e.g., crystal oscillators), only components at the oscillation frequency (i.e., the fundamental, in this case) are significant; higher harmonics can be ignored, because the high-Q tank eventually suppresses them somewhere in the loop [35], [36]. Thus, under large amplitude conditions, the motional resistance of the μmechanical resonator seen within the positive feedback loop is effectively given by [35]

$$R_{x12(1)} = -\frac{v_{1(1)}}{i_{2(1)}} \tag{20}$$

where $v_{1(1)}$ is the amplitude of the fundamental component of voltage applied across the resistor and $i_{2(1)}$ is the amplitude of the resulting fundamental component of current, with distortion harmonics $i_{2(2)}$, $i_{2(3)}$, etc., ignored (and where parentheses denote the harmonic in question).

Fig. 9 shows the circuit schematic for this oscillator. The sustaining amplifier design is transresistance, using shunt–shunt feedback to achieve low input resistance, and therefore, minimal Q loading. M_4 and M_5 serve as replica biasing for gain stages M_1–M_3 and M_6–M_7. The first stage $(M_1$–$M_3)$ provides transresistance gain a_{r1}. Here, M_3 is biased in the linear region by control voltage V_{GC} and serves as an MOS resistor with small-signal resistance approximately given by

$$R_3 = \left[\mu_n C_{\text{ox}} \left(\frac{W}{L}\right)_3 (V_{\text{GC}} - V_{G1} - V_{t3})\right]^{-1} \tag{21}$$

where μ_n is the electron mobility in silicon, C_{ox} is the gate-oxide capacitance per unit area, W and L are the MOS channel width and length, respectively, V_{G1} is the voltage at the gate of M_1, and V_{t3} is the threshold voltage of M_3. M_{3A} is also an MOS resistor to be used for startup in automatic-level control applications. Capacitor C_{c1} serves to compensate the first-stage feedback loop. For the first stage, $a_{r1} = -R_3$.

The second stage of the amplifier $(M_6$–$M_7)$ is a common-source amplifier, providing additional voltage gain a_{v2}. The output of this second stage is directly connected to the μresonator input, without the use of a resistance-lowering source follower. This was originally intended as a power-saving feature in a subthreshold version of this oscillator. In retrospect, however, a source follower should have been included to lower the output resistance of this second stage, so as to minimize the Q-loading on the μresonator.

The transresistance gain R_{amp} of the whole amplifier is given by

$$R_{\text{amp}} = a_{v2} a_{r1} = g_{m7}(r_{o7} \| r_{o6}) R_3 \tag{22}$$

where g_{m7} is the transconductance of M_7 and r_{o6} and r_{o7} are the incremental output resistances of M_6 and M_7, respectively. To insure startup of oscillation, the gain R_{amp} should be chosen two or more times larger than $(R_{x12} + R_i + R_o)$. For the μresonator summarized in Tables I and II, $R_{\text{amp}} \approx 5.86$ MΩ is a safe choice. The sustaining amplifier was designed for $R_{\text{amp}} = 5.5$ MΩ when $V_{\text{GC}} = 2.5$ V. The value of R_{amp} is also adjustable through V_{GC}, as seen by combination of (21) and (22). Table III presents data for the designed sustaining amplifier.

To minimize frequency deviation due to phase lag, the bandwidth of the sustaining transresistance amplifier should be chosen at least ten times larger than the oscillation frequency.

TABLE III
SUSTAINING TRANSRESISTANCE AMPLIFIER DATA

Parameter	Value	Units
$\mu_n C_{ox}$	35	$\mu A/V^2$
$\mu_p C_{ox}$	15	$\mu A/V^2$
Threshold Voltage, $V_{tn} = \lvert V_{tp} \rvert$	0.7	V
$g_{m1}=g_{m5}=g_{m7}=g_{mn}$	6.78×10^{-5}	Ω^{-1}
$g_{m2}=g_{m4}=g_{m6}=g_{mp}$	6.50×10^{-5}	Ω^{-1}
Gate Oxide Thickness, t_{ox}	500	Å
C_{gs1} (for M_1 in saturation)	20.6	fF
$(W/L)_1=(W/L)_5=(W/L)_7=(W/L)_n$	7/7	µm/µm
$(W/L)_2=(W/L)_4=(W/L)_6=(W/L)_p$	8/4	µm/µm
$(W/L)_3=(W/L)_{3A}$	5/80	µm/µm
1st Stage Transresistance Gain, a_{r1}	280,000*	Ω
Input Resistance, R_i	40	kΩ
Output Resistance, R_o	1.65	MΩ
2nd Stage Voltage Gain, a_{v2}	20*	V/V
Overall Transresistance Gain, R_{amp}	5.5×10^6*	Ω
3dB Bandwidth	12.7†	MHz

*Gain determined for V_{GC}=2.5V, V_{DD}=2.5V, V_{SS}=−2.5V.
†Determined with loading by µresonator port 1.

The 3-dB bandwidth for this amplifier is determined by either the transresistance stage (M_1–M_3) or the voltage gain stage (M_6–M_7), whichever has the lower frequency. For the design of this work, where $a_{r1} < 400$ kΩ, the second stage normally limits the 3-dB frequency. For this case

$$\omega_{-3\text{ dB}} = \left\{ \frac{1}{g_{m1}} [C_{\text{gd7}}(1 + a_{v2}) + C_{G7}] + C_L(r_{o6} \| r_{o7}) \right\}^{-1} \tag{23}$$

where g_{m1} is the transconductance of M_1, C_{gd7} is the gate-to-drain capacitance of M_7, C_{G7} is the total capacitance in shunt with the gate of M_7, and C_L is the total capacitance loading the drain of M_7, including μresonator input capacitance C_{o1}. The second term in (23) normally dominates.

The output amplifier, fed by port 3 of the μmechanical resonator, is composed of a replica of the sustaining amplifier (M_9–M_{12}) and a unity-gain buffer (M_{13}–M_{19}) designed to drive off-chip loads.

IV. FABRICATION

The technology for the fully monolithic high-Q oscillator combines planar CMOS processing with surface micromachining [39]. The technologies are combined in a modular fashion, in which the CMOS processing and surface micromachining are done in separate process modules, with no intermixing of CMOS or micromachining steps. This modular integration of CMOS and microstructures (MICS) process has the advantage that it allows the use of nearly any CMOS process with a variety of surface-micromachining processes.

To avoid problems with microstructure topography, which commonly includes step heights of 2–3 μm, the CMOS module is fabricated before the microstructure module. Although this solves topography problems, it introduces constraints on the CMOS. Specifically, the metallization and contacts for the electronics must be able to survive post-CMOS micromachining processing with temperatures up to 835°C. Aluminum interconnect, the industry standard, cannot survive these temperatures. For this reason, tungsten with $TiSi_2$ contact barriers is used as interconnect for this process.

A cross-sectional outline of the MICS process sequence is presented in Fig. 10. The fabrication process begins with standard CMOS up to and including the contact cut for the first metallization [Fig. 10(a)]. At this point, a thin film of titanium is sputter deposited onto the wafer surface and then rapid-thermal annealed (RTA) for 30 s at 600°C in a nitrogen ambient to form $TiSi_2$ at points where titanium contacts silicon. Unreacted titanium is then etched away using a 3 : 1 $NH_4OH : H_2O_2$ solution, and another RTA is performed for 10 s at 1000°C to activate dopants. At this point, the cross section appears as in Fig. 10(b). A 6000-Å film of tungsten is then sputter deposited and patterned to form the single-level interconnect [Fig. 10(c)]. Subsequent low-pressure chemical vapor depositions (LPCVD's) of 5000 Å of low-temperature oxide (LTO) and 1500 Å of silicon-rich nitride at 450 and 835°C, respectively, serve to passivate the metal [Fig. 10(d)].

Vias are then plasma etched through the nitride and underlying oxide to expose gate polysilicon runners that were formed during CMOS processing [Fig. 10(e)]. These runners serve as an intermediate conductive level that joins the CMOS tungsten interconnect with the structural polysilicon interconnect. Direct contact between the first structural (ground plane) polysilicon and tungsten metal never occurs. This originally was a precaution to prevent contamination of the polysilicon deposition system by tungsten.

Next, 3000 Å of *in situ* phosphorous-doped LPCVD polysilicon is deposited at 610°C and patterned to define the interconnect and ground-plane polysilicon for the microstructures [Fig. 10(f)]. This is followed by a 2-μm LPCVD deposition (450°C) of phosphosilicate glass (PSG) that serves as a sacrificial layer to be removed when releasing the mechanical structures. Next, a contact cut in the PSG defines the anchor points for resonators and electrodes [Fig. 10(g)], and 2 μm of *in situ* phosphorous-doped LPCVD polysilicon is deposited at 610°C to serve as the structural material.

The structural material is then capped with a 5000-Å film of LTO, which serves as a hard mask during etching of the structural polysilicon. Use of this oxide mask greatly enhances the resolution with which finger gaps may be defined. Without the oxide mask, a double or triple layer of photoresist would be required to insure proper coverage of large steps, which occur around the anchors of the resonators and electrodes. With an oxide mask, however, photoresist step coverage is no longer necessary if anisotropic dry etching is to be used, since the conformal oxide layer is much thicker vertically along steep slopes where the photoresist is thinnest. A much thinner film of photoresist may be used, which leads to improved lithographic resolution. High resolution is extremely important for oscillator or signal-processing applications of capacitively transduced resonators, since the degree of electromechanical coupling achievable via capacitive transduction is directly related to the gap spacings between interdigitated fingers.

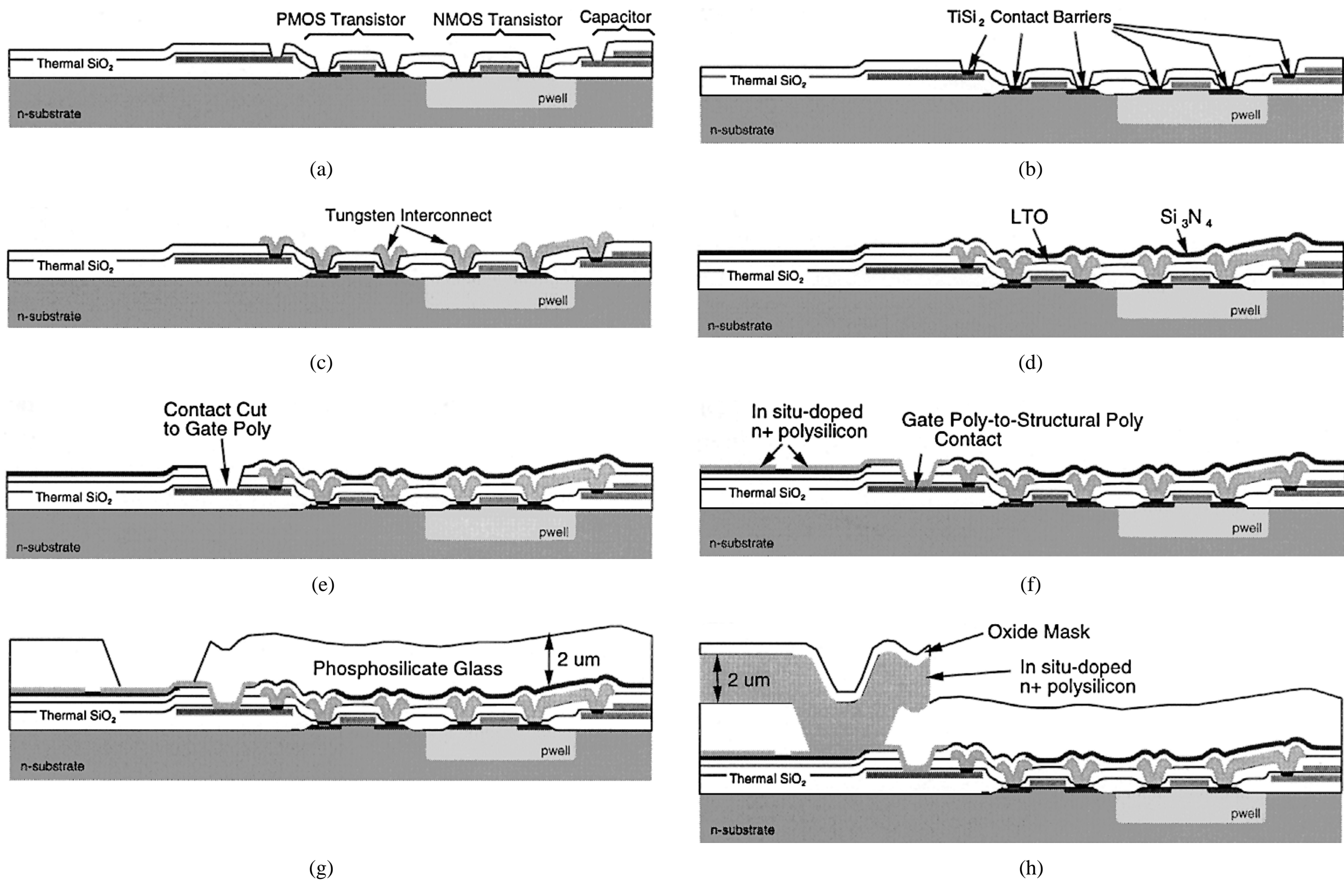

Fig. 10. Cross-sectional process flow for the CMOS plus microstructures fabrication technology. (a)–(c) constitute the metallization steps, (d)–(f) present the circuit-to-structure interface, and (g)–(h) show the micromachining steps. The final cross section is presented in Fig. 11.

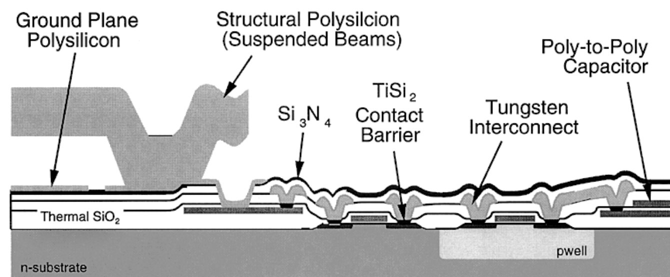

Fig. 11. Final cross section of the CMOS plus microstructures process used in this work.

The thin layer of photoresist is patterned with a single mask to define resonator geometries, including interdigitated-comb fingers. The oxide cap is first plasma etched using a CF_4/C_2F_6-based chemistry. It then serves as a hard mask for the ensuing polysilicon plasma etch, which is done using a Cl_2-based chemistry, and which results in the cross section of Fig. 10(h). Next, a stress anneal is performed via RTA for 1 min at 950°C, followed by a sequence of etches to expose the conductive backside of the silicon wafer. Last, the wafer is dipped in 5 : 1 buffered hydrofluoric acid to remove the sacrificial PSG and free the microstructures. The wafers are dried using a supercritical carbon-dioxide technique, which prevents sticking of the structures to the substrate by eliminating surface tension forces during drying [40]. The final cross section is shown in Fig. 11. Fig. 12 shows an overhead-view SEM of the completed 16.5-kHz prototype CMOS μresonator oscillator.

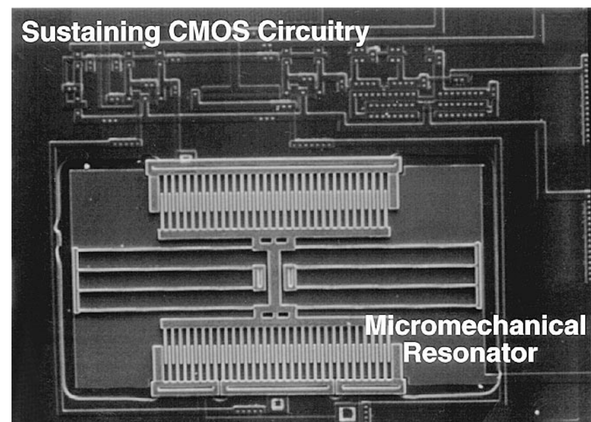

Fig. 12. SEM of the 16.5-kHz CMOS μresonator oscillator. The μresonator occupies $420 \times 230\ \mu m^2$.

Although a deviation from the popular one hour at 1050°C furnace stress anneal [12], which cannot be used here due to the presence of CMOS electronics, the rapid thermal stress anneal performed acceptably. However, due to the heavy phosphorous concentration in the polycrystalline silicon, the residual compressive stress in the polysilicon films of this work was still quite large and was difficult to anneal away. Thus, stress-relaxing designs, such as cantilevers or folded-

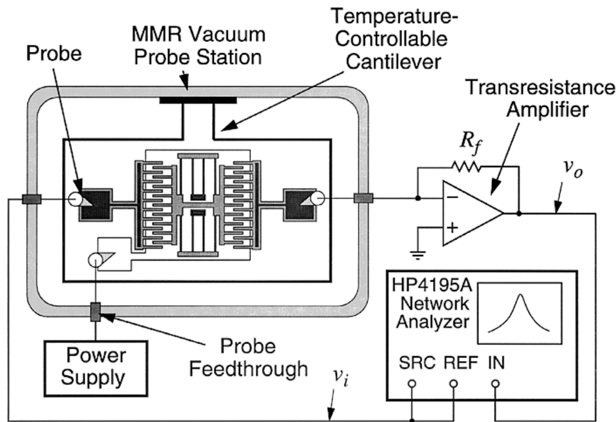

Fig. 13. Experimental setup used to characterize μmechanical resonators that yielded Figs. 4–7.

beam resonators, were required for oscillators fabricated via this process. More recent work, however, shows that the aforementioned stress problems may be alleviated by adjusting the temperature and the PH_3/SiH_4 mol ratio during polysilicon deposition [41]. An alternative solution might be the use of *in situ* boron-doped polysilicon, which has the additional advantage of substantially increasing the polysilicon deposition rate.

V. Experimental Results and Discussion

Design data for the prototype μmechanical resonator oscillator are summarized in Tables I–III. This oscillator was verified through SPICE simulation, then fabricated using the process detailed in Section IV.

The fabricated oscillator and associated stand-alone resonators were bonded up in dual-in-line packages and tested under a variable-pressure vacuum probe station. To characterize the stand-alone resonators, the experimental setup of Fig. 13 was utilized. Here, an MMR Technologies cold chuck probe station is used, in which passive resonators are suspended on a temperature-controllable cantilever in a vacuum chamber capable of achieving pressures on the order of 5 μtorr. Resonator electrodes are accessed via probes, and resonance is excited and detected using an HP 4195A network/spectrum analyzer and an off-chip transresistance amplifier. Since the μresonator being characterized is a high-Q element, extreme precautions to guard against parasitic feedthrough interference are not required [18]. Figs. 4–7 were obtained using this setup.

As seen from Table I, the measured and calculated resonance frequencies for the μresonator used in the oscillator differ by about 2.4%. Only one run was successfully completed for this work, so the run-to-run variance in frequency cannot be evaluated here. However, the frequency-mismatch tolerance was measurable and was found to be about 0.4% for a group of identical resonators in close proximity, and only slightly higher (~0.5%) from die to die. Since variations in thickness h do not heavily impact the resonance frequency of this resonator design [i.e., h cancels to first order in (1)], the observed frequency mismatch is perhaps best attributed to inconsistencies in lithography and etching. Possible strategies for correcting absolute frequency tolerances include laser trimming or frequency adjustment via a recent electrically activated localized annealing technique [19]. Voltage-controllable tuning via electrical spring stiffnesses (k_e's) is also possible if slight nonlinearities are introduced into comb-capacitor geometries.

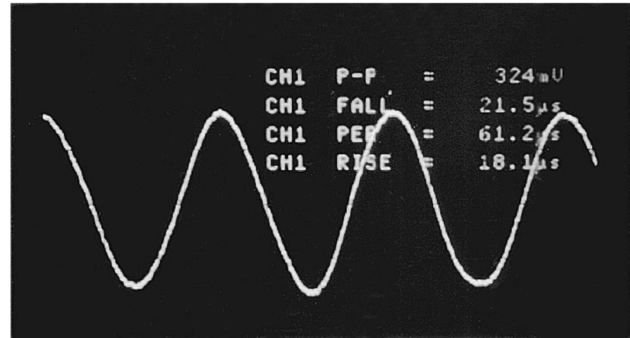

Fig. 14. Oscilloscope waveform for the prototype μresonator oscillator.

To test the oscillator itself, the MMR probe station is again used to achieve appropriate vacuum, with bias voltages applied via a combination of probes and electrical feedthroughs, and with the oscillator output now delivered by the on-chip buffer to an oscilloscope or to an HP3561A dynamic signal analyzer. Fig. 14 shows a typical oscilloscope plot for a 16.5-kHz version of this oscillator measured under a vacuum pressure of 20 mtorr.

A. Amplitude Limiting

As mentioned in Section III, the oscillation amplitude of a high-Q oscillator circuit builds up until some form of nonlinearity reduces the overall loop gain A_l to unity (or slightly above), at which point the amplitude stabilizes at some steady-state value. For oscillators controlled by quartz crystals, the nonlinearity that limits amplitude usually appears in the sustaining circuit, where MOS transistors enter the triode region at large voltage amplitudes, reducing effective device transconductances until the loop gain drops to unity. Limiting due to crystal nonlinearity is rare, since quartz crystal units display very little transducer nonlinearity over normal oscillator operating voltage ranges [37].

On the other hand, as seen in Fig. 14, the oscillators of this work reach steady state at voltage amplitudes of tens to hundreds of millivolts, well within the linear range of the sustaining amplifier. Furthermore, the oscillation amplitude is observed to be strongly dependent upon the dc bias V_P applied to the resonator, as shown in Fig. 15, which plots steady-state oscillation amplitude versus dc bias V_P for the fabricated oscillator under conditions yielding the parameter values summarized in Tables I and III. The tiny magnitude of steady-state oscillation amplitude and its dependence on dc bias suggest that nonlinearities associated with the micromechanical resonator dominate the limiting process. As explained in [38], the stiffness (Duffing) nonlinearity depicted in Fig. 6 is not a likely cause for limiting, since stiffness is a nondissipative quantity. Rather, some form of *nonlinear damping*

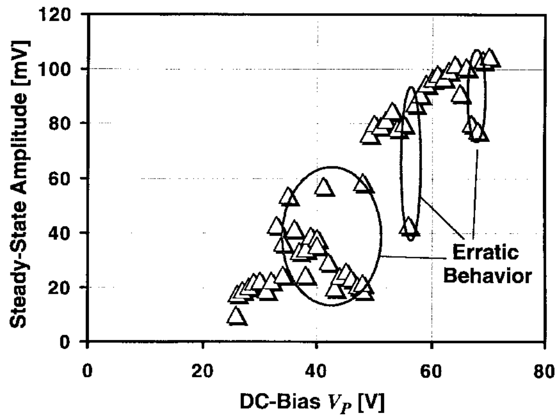

Fig. 15. Plot of steady-state amplitude versus resonator dc bias V_P measured under the conditions of Tables I and III. Although stable operation is seen under the majority of dc biases tested, there are some areas where erratic behavior is seen. (See text.)

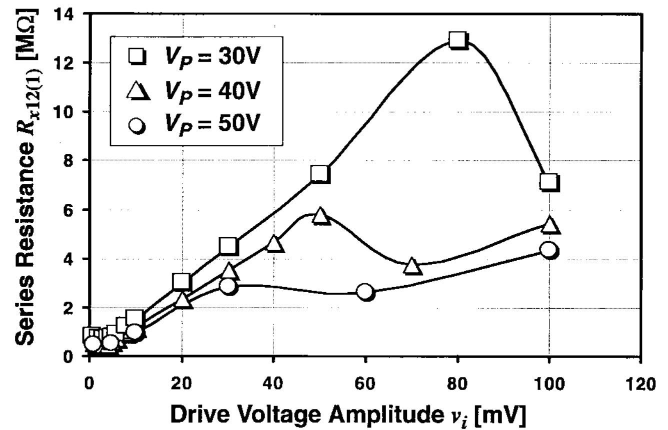

Fig. 16. Plot of $R_{x12(1)}$ versus drive voltage amplitude v_i for varying values of resonator dc bias V_P.

that induces a variation of resonator series motional resistance R_{x12} with input amplitude v_i is most likely responsible.

To identify the functional nonlinearity, the Bode plot transfer functions of a stand-alone resonator were measured with varying values of dc bias V_P and input voltage amplitude v_i, using the setup of Fig. 13 under environmental conditions identical to those used for determination of Fig. 15. A sample plot of transfer functions for $V_P = 30$ V and for increasing values of v_i was previously shown in Fig. 6. For each measurement, the network analyzer frequency was swept in the upward direction to obtain the peak amplitude in the stiffening Duffing curve, where the resonator voltage-to-current phase shift is appropriate for oscillation. Equivalent series motional resistances $R_{x12(1)}$ were then calculated for these peak amplitudes using the expression (referring to Fig. 13)

$$R_{x12(1)} = \frac{R_f}{|v_{o(1)}/v_i|} \tag{24}$$

where $R_f = 100$ kΩ for these measurements. Note that, as implied by nomenclature in (24), the $R_{x12(1)}$'s determined using this procedure are effectively those defined by (20), since the HP4195A used for the measurements filters out frequency components different from the fundamental driving component, and thus measures only the fundamental of the output. $R_{x12(1)}$'s determined using this procedure are plotted versus input voltage amplitude v_i for varying values of V_P in Fig. 16. These plots indicate a strong dependence of $R_{x12(1)}$ on input voltage amplitude, suggesting significant nonlinearity in the transfer functions of capacitive comb-transduced micromechanical resonators. Given that steady-state oscillation occurs when $R_{x12(1)} = (R_{\text{amp}} - R_i - R_o) = 3.81$ MΩ, the plots are also consistent with Fig. 15, predicting oscillation amplitudes of 25 mV for $V_P = 30$ V, 33 mV for $V_P = 40$ V, and 75 mV for $V_P = 50$ V—all very close to the measured values in Fig. 15.

To determine the physical source of nonlinearity, it is helpful to derive the basic differential equation governing overall oscillator operation. For this purpose, we start with the equation of motion for this system, given by

$$m_r\,\ddot{x} + c_r\,\dot{x} + k_{r1}\,x + k_{r3}\,x^3 = f_d \tag{25}$$

where m_r is the effective mass of the μmechanical resonator, c_r is the damping coefficient, k_{r1} and k_{r3} are stiffness coefficients modeling stiffening Duffing nonlinearity, and f_d is the net force applied to the resonator. Using (2) and (3), the net force can be expanded into

$$f_d = V_P^2 N_{g1} N_{g2} \left(\frac{\partial C}{\partial x}\right)^2_{\text{sov}} R_{a\text{eff}}\dot{x} \tag{26}$$

where $(\partial C/\partial x)_{\text{sov}}$ corresponds to a single finger overlap and $R_{a\text{eff}} = R_{amp} - R_i - R_o$. Again, since this is a high-Q oscillator system, (26) can be used for both small and large amplitude operation, provided that expressions used to determine relevant parameters [such as $(\partial C/\partial x)_{\text{sov}}$] for large amplitude operation use fundamental components, as was done in association with (19) and (20). Inserting (26) in (25) and rearranging, the basic oscillator equation is found to be

$$m_r\,\ddot{x} + \left[\underbrace{\frac{\omega_o m_r}{Q} - V_P^2\,N_{g1}\,N_{g2}\left(\frac{\partial C}{\partial x}\right)^2_{sov} R_{a\text{eff}}}_{\text{damping coefficient}}\right]\dot{x} + k_{r1}\,x + k_{r3}\,x^3 = 0. \tag{27}$$

For proper startup, an oscillator should be designed to have negative damping initially; i.e., the damping coefficient in (27) should be negative at turn on. With negative damping, the system is unstable, and oscillations build up until some form of nonlinearity (e.g., a change in one of the variables in the damping coefficient) forces the damping coefficient to zero, at which point steady-state oscillation is achieved.

Of the terms in the damping coefficient of (27), only Q and $(\partial C/\partial x)_{\text{sov}}$ can change appreciably as the oscillation amplitude increases. ($R_{a\text{eff}}$ can change with increasing oscillation voltage, but not significantly at millivolt signal levels.) Initial measurements indicate that Q is not strongly dependent on vibration amplitude for folded-beam, comb-driven resonators, at least not for micrometer-scale displacements. In addition, the values of Q as a function of v_i required to match the curves of Fig. 16 [assuming $(\partial C/\partial x)_{\text{sov}}$ remained constant] are inconsistent with actual displacement amplitude data over the majority of the drive amplitude range. Although this

does not necessarily rule out Q variation with amplitude as a possible mechanism, it does leave nonlinear variation in $(\partial C/\partial x)$ with vibration amplitude as the most likely mechanism for amplitude limiting of this oscillator. Thus, although comb transducers do greatly linearize the resonator-to-electrode capacitance as a function of displacement over their parallel-plate capacitor counterparts, it seems that non-idealities, e.g., levitation [20] and end effects [13], can still generate enough nonlinearity in $C_n(x)$ to instigate oscillator limiting.

Using the data from Fig. 16 and from Table I, assuming tentatively that $(\partial C/\partial x)$ nonlinearity is largely responsible for R_{x12} variation, and using an expression for "large signal" $(\partial C/\partial x)_{\rm sov(1)}$

$$\left(\frac{\partial C}{\partial x}\right)_{\rm sov(1)} = \left[\frac{\sqrt{k_r m_r}}{Q V_P^2 N_{g1} N_{g2} R_{x12(1)}}\right]^{1/2}. \quad (28)$$

Fig. 17 plots $(\partial C/\partial x)_{\rm sov(1)}$ versus input voltage amplitude for varying values of dc bias V_P. At low drive voltage amplitudes, the $(\partial C/\partial x)_{\rm sov(1)}$ curves exhibit excessive nonlinearity, actually peaking at specific values of drive voltage for each V_P tested. For large values of drive voltage, the curve is seen to level off, approaching a horizontal asymptote. This limiting behavior for large values of drive voltage is expected, since the micromechanical resonators of this work were defensively designed such that the shuttle hits the anchors first, before the shuttle fingers touch the electrodes (which would destroy the device due to the large voltage drop between the shuttle and electrodes). Thus, for drive voltages larger than a certain V_P-dependent threshold, the μresonator vibration amplitude remains fixed to the initial (static) distance between anchor and shuttle, $d_{\rm sa} = 16$ μm (see Fig. 1), and $(\partial C/\partial x)_{\rm sov(1)}$ stabilizes, as seen in Fig. 17. This model where $(\partial C/\partial x)$ nonlinearity dominates the oscillator limiting process is further supported by the fact that the $(\partial C/\partial x)_{\rm sov(1)}$data in Fig. 17 are consistent with visually estimated displacement amplitude data up to the point when the shuttle hits the anchors. After reaching this maximum amplitude, Q variations due to energy loss on impact with the anchors begin to also influence the oscillator output amplitude.

Given the degree of nonlinearity shown in Figs. 16 and 17, it is not surprising that the plot of oscillation amplitude versus dc bias voltage in Fig. 15 is discontinuous and somewhat erratic at several points. In particular, for V_P's from 30 to 33 V, the μresonator vibration was visually erratic (as seen under a microscope), and sidebands appeared in its Fourier spectrum, as shown in Fig. 18. At $V_P = 38$ and 48 V, the oscillation was observed to jump between up to three different frequencies and amplitudes. At V_P's between 40 and 48 V, the resonance was visually erratic, and its Fourier peak as seen on a spectrum analyzer broadened significantly, spectrally indicating a loss in stability. The range of instability varied for different oscillators and operating environments, some exhibiting much less erratic behavior than in Fig. 15, with stable operation over sizeable ranges of V_P. Nevertheless, for virtually all oscillators tested, erratic behavior could always be induced at some value or range of V_P.

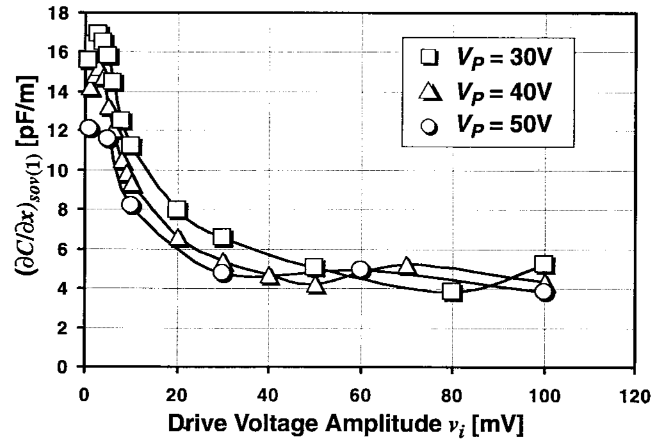

Fig. 17. Plot of $(\partial C/\partial x)$ (for a single finger overlap) versus drive voltage amplitude v_i for varying values of resonator dc bias V_P, determined using the data of Fig. 16 and assuming Q remains constant with drive amplitude.

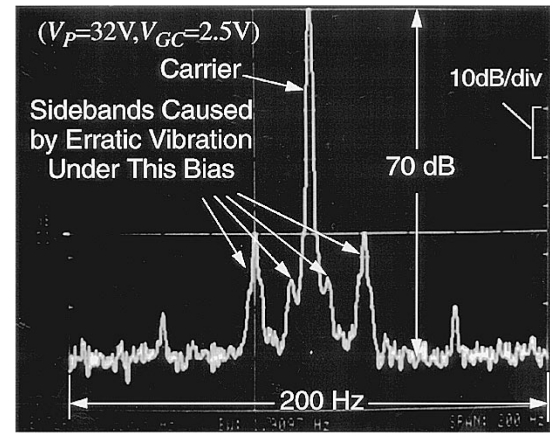

Fig. 18. Output spectrum for the μresonator oscillator as measured by an HP 3561A dynamic signal analyzer under biasing conditions ($V_P = 32$ V) where the μresonator is visually observed to vibrate erratically. Under this particular bias arrangement, sidebands appear around the carrier peak.

For these reasons, the use of resonator nonlinearity for amplitude limiting is deemed risky if oscillator predictability and stability is desired. Rather, automatic level control (ALC) circuitry should be utilized for more precise control of oscillation amplitude. The circuit of Fig. 9, in fact, is designed to allow for ALC, since its gain is controllable by the voltage $V_{\rm GC}$ at the gate of MOS resistor M_3. Specifically, ALC can be realized by routing the drain voltages of M_6 and M_7 through a peak detector, then a comparator, then back to the gate of M_3. In Fig. 9, M_{3A} is placed in parallel with M_3 to insure oscillator startup in the presence of an ALC loop.

B. Phase Noise

One important figure of merit for oscillators, particularly those used in communications applications, is the phase noise power present at frequencies close to the carrier frequency. Phase noise requirements are typically expressed as noise-to-carrier power ratios in dBc/Hz at specific offset frequencies from the carrier. For example, the phase noise requirement for a 10-MHz crystal reference oscillator in a wireless phone might be given at three offset frequencies: −90 dBc/Hz

maximum at a 10-Hz carrier offset, −110 dBc/Hz at 100-Hz offset, and −130 dBc/Hz at 1-kHz offset. If extrapolated down to the 16.5-kHz frequency of the present μresonator oscillator by matching percent offsets, this specification becomes −90 dBc/Hz at 0.0165-Hz offset, −110 dBc/Hz at 0.165-Hz offset, and −130 dBc/Hz at 1.65-Hz offset. We acknowledge that this matching of percent offsets does not comprise a rigorous specification. In fact, a specification that retains the same offset frequencies and reduces associated dBc/Hz levels by a factor of (10 MHz/16.5 kHz)^2 would be more correct if a 16.5-kHz oscillator were to actually be used in a transceiver. However, there is no intent here to use a 16.5-kHz oscillator for an actual transceiver application; rather, this is an experimental oscillator that preludes 10-MHz versions to come. Thus, we will adhere to the first extrapolated specification above, since this better conveys the potential performance of an oscillator referenced to a 10-MHz μresonator with comparable Q and power-handling ability.

The most commonly recognized cause of phase noise is superposed and aliased electronic noise from the sustaining amplifier [42]. For the case of μresonator oscillators, however, noise contributions from Brownian motion of the μmechanical resonator (as modeled by the value of R_{x12}) must also be considered, in addition to those due to the sustaining amplifier. Via appropriate feedback analysis, and with the recognition that the output power of an oscillator is merely amplified noise within a feedback-reduced bandwidth, the phase noise-to-carrier power ratio at an offset frequency f_m from the carrier at f_o is given by an expression similar to that originally derived by Leeson [42], [43]

$$L\{f_m\} = 10\ \log\left\{\frac{2kT[1+\alpha F]}{P_o}\cdot\frac{R_{\rm tot}}{R_{x12(1)}}\cdot\left[1+\left(\frac{f_o}{2Qf_m}\right)^2\right]\right\} \quad (29)$$

where $R_{x12(1)} = R_{amp} - R_i - R_o$ and $R_{\rm tot} = R_{\rm amp}$ in steady state, $P_o = (1/2)i_o^2 R_{\rm tot}$ is the carrier output power, i_o is the current delivered by the output port of the μresonator (i.e., port 2), α is a modification factor given by

$$\alpha = \zeta\left(1+\frac{R_i+R_o}{R_{x12(1)}}\right) \quad (30)$$

that accounts for impedance mismatches and unity loop gain operation of the amplifier, $\zeta = 1$ for this linearly operating sustaining amplifier, and F is a noise factor associated with the sustaining amplifier similar to that in [44] and for this oscillator given by

$$F = \frac{R_{\rm amp}}{R_{\rm noise}} \quad (31)$$

where

$$\frac{1}{R_{\rm noise}} = \frac{\overline{i_{R_{\rm amp}}^2}}{4kT\Delta f} = \frac{1}{R_3} + \left(\omega_o^2 C_{\rm gs1}^2 + \frac{1}{R_3^2}\right)\frac{\overline{v_{\rm ia}^2}}{4kT\Delta f} \quad (32)$$

and

$$\frac{\overline{v_{\rm ia}^2}}{\Delta f} = 4kT\,\frac{2}{3}\left(\frac{2}{g_{\rm mn}}+\frac{2}{g_{\rm mp}}\right) + \left(\frac{2K_{\rm fn}}{W_nL_nC_{\rm ox}}+\frac{2K_{\rm fp}}{W_pL_pC_{\rm ox}}\right)\frac{1}{f_o} \quad (33)$$

where $\overline{i_{R_{\rm amp}}^2}$ represents the input-referred current noise of the sustaining amplifier, $K_{\rm fn}$ and $K_{\rm fp}$ are flicker-noise coefficients for NMOS and PMOS devices, respectively, $C_{\rm gs1}$ is the gate-to-source capacitance of M_1 in saturation, and R_3 is given by (21). Note that (29) represents an *approximate* expression that accounts for only $1/f^2$ noise and white noise at large offsets.

Fig. 19 plots $L\{f_m\}$ versus offset frequency f_m for several values of V_P and $V_{\rm GC}$ using (29) with data summarized in Figs. 15 and 17 and Tables I and III, and with $K_{\rm fn} = K_{\rm fp} = 3\times 10^{-24}$ V^{2}F. The performance of the actual oscillator (as seen in the top four curves) in Fig. 19 is well short of the extrapolated specification given earlier in this subsection (and shown as a dotted line in the figure). There are two main reasons for this.

1) Given the large gate-oxide thickness $t_{\rm ox}$ in this conservative CMOS process, flicker-noise components dominate the value of (31) at the 16.5-kHz frequency of this oscillator, substantially degrading its performance (by ∼9 dBc/Hz).
2) The output power of this oscillator is severely limited by the power-handling/generating capability of the μmechanical resonator.

Given that flicker noise in the first item can be attenuated by choosing larger device sizes, and considering the direct dependence of (29) on output power P_o, the second item above is by far the most serious limitation. In particular, under the amplifier bias conditions of Table III, for V_P's of 30, 40, and 50 V, resonator output currents of 4.5, 11.2, and 13.6 nA, respectively, were observed, corresponding to output powers of 58 pW, 0.28 nW, and 0.52 nW. (Note that at $V_P = 50$ V, the μresonator shuttle is already hitting its anchors.) Such tiny output powers severely limit the short-term stability of this oscillator, rendering it incapable of achieving the needed phase noise performance, despite the high Q of its reference μresonator.

A formal phase noise measurement was not possible for this oscillator due to the unavailability of a commercial measurement system for oscillator carrier frequencies below 20 kHz. Instead, limited insight into the stability (or lack of stability) of this oscillator was obtained through observation of its output spectrum on an HP 3561A dynamic signal analyzer. Using this approach, the magnitude of the oscillation peak for this oscillator was observed to rise with V_P, and its peak and thermal noise levels as seen from Fig. 18 (ignoring the sidebands) were consistent with the values of Fig. 19 at large offsets. The output peak was thinnest, highest, and most stable at the largest applied value of resonator bias ($V_P = 140$ V), at which the shuttle was clearly hitting the anchors when observed under a microscope. Given the possibility of fatigue and fracture, such an operation mode is admittedly not acceptable for actual applications. Nevertheless, under these conditions,

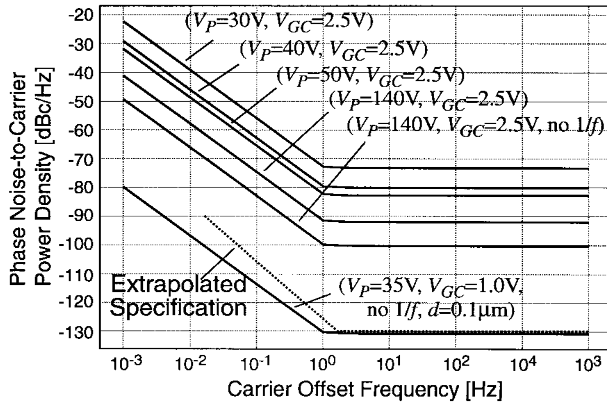

Fig. 19. Simulated phase noise performance for the 16.5-kHz μmechanical resonator oscillator under various values of V_P and $V_{\rm GC}$, and with both actual (top four curves) and exploratory circuit and resonator conditions.

the oscillator exhibited its best performance, which at large offsets was consistent with that of the ($V_P = 140$ V, $V_{\rm GC} = 2.5$ V) curve of Fig. 19, but which still was not nearly good enough to satisfy the extrapolated specifications given earlier. It should be noted that the associated curve in Fig. 19 was generated with the recognition that the resonator shuttle was impacting its anchors, so its output current was determined using the expression

$$i_o = V_P \frac{\partial C_2}{\partial x} \omega_o X_{\max} \tag{34}$$

where $\partial C_2/\partial x = (30)(5 \times 10^{-12}) = 1.5 \times 10^{-10}$ F/m and the static shuttle-to-anchor distance $X_{\max} = d_{\rm sa} = 16$ μm. With $V_P = 140$ V, (34) yields $i_o = 34.8$ nA.

C. Improving Short-Term Stability

Even with enormous values of bias voltage and with the resonator shuttle hitting its anchors—an admittedly inappropriate mode of operation—the short-term stability demonstrated here falls well short of the extrapolated specifications. With a few modifications, however, this oscillator can be made to meet these specifications (at least in theory).

In particular, in a more modern CMOS process, the gate-oxide thickness $t_{\rm ox}$ is many times smaller, so flicker noise would be much reduced. Flicker noise would also be further suppressed at the 10-MHz frequency of an actual communications reference oscillator. Thus, in a commercial oscillator, limitation (1) would not be an issue.

To improve the power handling and generating capability of the resonator, $\partial C_1/\partial x$ should be reduced, perhaps by using only one or two fingers at port 1, and $\partial C_2/\partial x$ should be maximized by using smaller finger-to-finger gaps. With a much reduced $\partial C_1/\partial x$, the μresonator can be driven by large input voltages without the shuttle's hitting the anchors. With a substantial increase in $\partial C_2/\partial x$, the output current i_o of the resonator is greatly increased, leading to much higher output power and orders of magnitude improvement in phase noise performance. Given that R_{x12} depends inversely upon the product of $\partial C_1/\partial x$ and $\partial C_2/\partial x$, decreases in $\partial C_1/\partial x$ and increases in $\partial C_2/\partial x$ can be chosen so that the value of R_{x12} remains relatively constant, so the gain of the sustaining amplifier required for startup need not change. On the other hand, an increase in gain via R_3 would be beneficial to the overall noise performance, as can be seen through (32).

To demonstrate the potential improvements afforded by the above strategies, Fig. 19 also includes a simulation using (29) that neglects flicker noise and that assumes a μresonator with 58 port 2 fingers having finger-to-finger gap spacings of 0.2 μm ($\partial C_2/\partial x = (10)(116)(5 \times 10^{-12}) = 5.8 \times 10^{-9}$ F/m), $V_P = 35$ V, $V_{\rm GC} = 1.0$ V to increase R_3, and $\partial C_1/\partial x$ chosen to allow limiting with an 18-μm shuttle displacement. As shown in Fig. 19, the simulated phase noise spectrum for this investigative design meets the extrapolated specification [at least theoretically, without considering $1/f^3$ noise, and recognizing that (29) is only an approximate formula].

Although they may seem so at first glance, the 0.2-μm finger-to-finger gap spacings in the above are not overly aggressive, and have in fact already been achieved in silicon via submicrometer lithography and inductively coupled high-density plasma etching [45]. However, the $V_P = 35$ V remains too high for most portable systems, so some strategy to increase the power output capability of μmechanical resonators is still needed. One of the most promising approaches to this end entails abandoning the comb-capacitive transducers of this work and instead using parallel-plate capacitive transducers, which provide substantially larger coupling magnitudes, can more easily achieve small capacitive gaps, and are better suited to implementation of high-frequency μresonators needed for communications applications [46]. However, as mentioned in Section II, supply-voltage sensitivity would still be an issue if this approach were adopted.

Even if the above power-handling issues were resolved, the ultimate stability of an oscillator referenced to a μmechanical resonator tank may still suffer from secondary phenomena related to their tiny size. For example, in addition to superposed electronic noise, any physical phenomenon that causes instantaneous frequency deviations of the resonator will contribute to the total phase noise power. Given that the typical mass of a μmechanical resonator is on the order of 10^{-11} kg, mass loading noise is expected to make a sizable contribution. Mass loading noise [47] arises from instantaneous differences in the rates of adsorption and desorption of contaminant molecules to and from the resonator surface, which cause mass fluctuations and consequently, frequency fluctuations. Some of the factors that determine the magnitude of mass loading noise include the adsorption/desorption rate of contaminant molecules, contaminant molecule size and weight, pressure, and temperature. Theory predicts that phase noise due to mass loading can be minimized by operating at certain optimal pressures and temperatures [10], [18], [47].

VI. Conclusions

Fully monolithic high-Q oscillators utilizing surface-micromachined polysilicon mechanical resonators have been designed, fabricated, and tested. Due to the novelty of the process and the devices, conservative measures were taken for the designs, and oscillators up to only 100 kHz were

fabricated. Designs up to a few megahertz are feasible using folded-beam resonator designs, and higher frequencies (tens of megahertz) should be feasible using more advanced designs aimed at maximizing resonator quality factor, which may otherwise degrade with increasing frequency (due to anchor dissipation and other frequency-dependent loss mechanisms [26]). Both material and architectural improvements should play important roles in maintaining μresonator Q. In addition, as frequency increases, smaller electrode-to-resonator gaps will be required at output ports to offset resonator stiffness increases and to maximize the power-generating capability of a given μmechanical resonator.

Due to both μresonator power-handling limitations and flicker-noise susceptibility at its low 16.5-kHz oscillation frequency, the phase noise level of this oscillator is not consistent with that of other high-Q references. The use of small and large electromechanical couplings at the input and output resonator transducers, respectively, has been proposed as one of several strategies to alleviate this problem. However, all things considered, this prototype oscillator, with its low oscillation frequency and its use of inefficient capacitive-comb transducers, is perhaps best suited to low-power time-keeper applications (e.g., wristwatches), and is not the best vehicle with which to evaluate the short-term stability of μmechanical resonator oscillators. Thus, although insights obtained via this oscillator concerning nonlinear limiting, μresonator circuit modeling, and oscillator startup modeling are valid, definitive conclusions concerning the ultimate short-term stability achievable by μmechanical resonator oscillators must await a more appropriate design—perhaps one at 10 MHz using advanced electromechanical coupling strategies. Such an oscillator is the subject of ongoing research.

Acknowledgment

The authors would like to thank S. Fang for assistance in CMOS fabrication as well as K. Voros and the staff of the Berkeley Microfabrication Laboratory for process support.

References

[1] E. A. Gerber and A. Ballato, Eds., *Precision Frequency Control—Vol. 1: Acoustic Resonators and Filters.* New York: Academic, 1985.

[2] E. Frian, S. Meszaros, M. Chuaci, and J. Wight, "Computer-aided design of square spiral transformers and inductors," in *1989 IEEE MTT-S Dig.,* pp. 661–664.

[3] N. M. Nguyen and R. G. Meyer, "Si IC-compatible inductors and LC passive filters," *IEEE J. Solid-State Circuits,* vol. 25, pp. 1028–1031, Aug. 1990.

[4] ——, "A 1.8-GHz monolithic LC voltage-controlled oscillator," *IEEE J. Solid-State Circuits,* vol. 27, no. 3, pp. 444–450, 1992.

[5] S. V. Krishnaswamy, J. Rosenbaum, S. Horwitz, C. Yale, and R. A. Moore, "Compact FBAR filters offer low-loss performance," *Microwaves RF,* pp. 127–136, Sept. 1991.

[6] R. Ruby and P. Merchant, "Micromachined thin film bulk acoustic resonators," in *Proc. 1994 IEEE Int. Frequency Control Symp.,* Boston, MA, June 1–3, 1994, pp. 135–138.

[7] C. T.-C. Nguyen and R. T. Howe, "Quality factor control for micromechanical resonators," in *Tech. Dig. IEEE Int. Electron Devices Meeting,* San Francisco, CA, Dec. 14–16, 1992, pp. 505–508.

[8] ——, "Microresonator frequency control and stabilization using an integrated micro oven," in *Dig. Tech. Papers 7th Int. Conf. Solid-State Sensors and Actuators (Transducers'93),* Yokohama, Japan, June 7–10, 1993, pp. 1040–1043.

[9] ——, "CMOS micromechanical resonator oscillator," in *Tech. Dig. IEEE Int. Electron Devices Meeting,* Washington, DC, Dec. 5–8, 1993, pp. 199–202.

[10] ——, "Design and performance of monolithic CMOS micromechanical resonator oscillators," in *Proc., 1994 IEEE Int. Frequency Control Symp.,* Boston, MA, May 31–June 3, 1994, pp. 127–134.

[11] R. T. Howe and R. S. Muller, "Resonant microbridge vapor sensor," *IEEE Trans. Electron Devices,* vol. ED-33, pp. 499–506, 1986.

[12] W. C. Tang, T.-C. H. Nguyen, and R. T. Howe, "Laterally driven polysilicon resonant microstructures," *Sensors Actuators,* vol. 20, pp. 25–32, 1989.

[13] M. W. Judy, "Micromechanisms using sidewall beams," Ph.D. dissertation, Dept. of Electrical Engineering and Computer Sciences, University of California at Berkeley, Apr. 1994.

[14] H. Nathanson, W. E. Newell, R. A. Wickstrom, and J. R. Davis, Jr., "The resonant gate transistor," *IEEE Trans. Electron Devices,* vol. ED-14, pp. 117–133, Mar. 1967.

[15] W. C. Tang, "Electrostatic comb drive for resonant sensor and actuator applications," Ph.D. dissertation, Dept. of Electrical Engineering and Computer Sciences, University of California, Berkeley, CA, Sept. 1989.

[16] W. A. Johnson and L. K. Warne, "Electrophysics of micromechanical comb actuators," *J. Microelectromechan. Syst.,* vol. 4, no. 1, pp. 49–59, Mar. 1995.

[17] L. Meirovitch, *Analytical Methods in Vibrations.* New York: Macmillan, 1967.

[18] C. T.-C. Nguyen, "Micromechanical signal processors," Ph.D. dissertation, Dept. of Electrical Engineering and Computer Sciences, University of California at Berkeley, Dec. 1994.

[19] K. Wang, A.-C. Wong, W.-T. Hsu, and C. T.-C. Nguyen, "Frequency-trimming and Q-factor enhancement of micromechanical resonators via localized filament annealing," in *Dig. Tech. Papers, 1997 Int. Conf. Solid-State Sensors and Actuators,* Chicago, IL, June 16–19, 1997, pp. 109–112.

[20] W. C. Tang, M. G. Lim, and R. T. Howe, "Electrostatic comb drive levitation and control method," *J. Microelectromechan. Syst.,* vol. 1, no. 4, pp. 170–178, Dec. 1992.

[21] P. R. Gray and R. G. Meyer, *Analysis and Design of Analog Integrated Circuits,* 2nd ed. New York: Wiley, 1984.

[22] M. Christen, "Air and gas damping of quartz tuning forks," *Sensors Actuators,* vol. 4, pp. 555–564, 1983.

[23] R. A. Buser, "Theoretical and experimental investigations of silicon single crystal resonant structures," Ph.D. thesis, Institute of Microtechnology, University of Neuchatel, Neuchatel, Switzerland, July 1989.

[24] Y.-H. Cho, A. P. Pisano, and R. T. Howe, "Viscous damping model for laterally oscillating microstructures," *J. Microelectromech. Syst.,* vol. 3, no. 2, pp. 81–87, June 1994.

[25] T. V. Rozhart, "The effect of thermoelastic internal friction on the Q of micromachined silicon resonators," in *IEEE Solid-State Sensor and Actuator Workshop Tech. Dig.,* Hilton Head, SC, June 4–7, 1990, pp. 13–16.

[26] V. B. Braginsky, V. P. Mitrofanov, and V. I. Panov, *Systems with Small Dissipation.* Chicago, IL: Univ. Chicago Press, 1985.

[27] S. Timoshenko, D. H. Young, and W. Weaver, Jr., *Vibration Problems in Engineering.* New York: Wiley, 1974.

[28] H. Guckel, D. W. Burns, H. A. C. Tilmons, DeRoo, and C. R. Rutigliano, "The mechanical properties of fine-grained polysilicon: The repeatability issue," in *IEEE Solid-State Sensor and Actuator Workshop Tech. Dig.,* Hilton Head Island, SC, June 1988, pp. 96–99.

[29] F. S. Crawford, "Elementary derivation of the law of equipartition of energy," *Amer. J. Phys.,* vol. 55, pp. 180–182, 1987.

[30] T. B. Gabrielson, "Fundamental noise limits in miniature acoustic and vibration sensors," Phase Rep. NADC-91113-50, Dec. 31, 1991.

[31] B. E. Boser and R. T. Howe, "Surface micromachined accelerometers," in *Proc. 17th Annu. Custom Integrated Circuits Conf.,* Santa Clara, CA, 1995, pp. 337–344.

[32] E. A. Gerber, A. Ballato, Eds., *Precision Frequency Control—Vol. 2: Oscillators and Standards.* New York: Academic, 1985.

[33] M. E. Frerking, *Crystal Oscillator Design and Temperature Compensation.* New York: Van Nostrand Reinhold, 1978.

[34] R. J. Matthys, *Crystal Oscillator Circuits.* New York: Wiley, 1983.

[35] E. A. Vittoz, M. G. R. DeGrauwe, and S. Bitz, "High-performance crystal oscillator circuits: Theory and application," *IEEE J. Solid-State Circuits,* vol. 23, pp. 774–783, June 1988.

[36] R. G. Meyer and D. C.-F. Soo, "MOS crystal oscillator design," *IEEE J. Solid-State Circuits,* vol. SC-15, pp. 222–228, Aug. 1980.

[37] F. L. Walls and J.-J. Gagnepain, "Environmental sensitivities of quartz oscillators," *IEEE Trans. Ultrason. Ferroelect., Freq. Contr.,* vol. 39, pp. 241–249, Mar. 1992.

[38] A. H. Nayfeh and D. T. Mook, *Nonlinear Oscillations.* New York: Wiley, 1979.

[39] W. Yun, R. T. Howe, and P. R. Gray, "Surface micromachined, digitally force-balanced accelerometer with integrated CMOS detection circuitry," in *IEEE Solid-State Sensor and Actuator Workshop Tech. Dig.*, Hilton Head Island, SC, June 22–5, 1992, pp. 126–131.

[40] G. T. Mulhern, D. S. Soane, and R. T. Howe, "Supercritical carbon dioxide drying of microstructures," in *Proc. 7th Int. Conf. Solid-State Sensors and Actuators (Transducers'93),* Yokohama, Japan, June 1993, pp. 296–299.

[41] M. Biebl, G. T. Mulhern, and R. T. Howe, "*In situ* phosphorous-doped polysilicon for integrated MEMS," in *Dig. Tech. Papers 8th Int. Conf. Solid-State Sensors and Actuators (Transducers'95),* Stockholm, Sweden, June 25–29, 1995, pp. 198–201.

[42] W. P. Robins, *Phase Noise in Signal Sources.* London: Peregrinus, 1982.

[43] D. B. Leeson, "A simple model of feedback oscillator noise spectrum," *Proc. IEEE,* vol. 54, pp. 329–330, Feb. 1966.

[44] J. Craninckx and M. Steyaert, "Low-noise voltage-controlled oscillators using enhanced LC-tanks," *IEEE J. Solid-State Circuits,* vol. 42, pp. 794–804, Dec. 1995.

[45] J. W. Weigold, W. H. Juan, and S. W. Pang, "Dry etching of deep Si trenches for released resonators in a Cl_2 plasma," *J. Electrochem. Soc.,* vol. 145, pp. 1767–1771, 1998.

[46] F. D. Bannon, III and C. T.-C. Nguyen, "High frequency microelectromechanical IF filters," in *Tech. Dig. 1996 IEEE Electron Devices Meeting,* San Francisco, CA, Dec. 8–11, 1996, pp. 773–776.

[47] Y. K. Yong and J. R. Vig, "Resonator surface contamination—A cause of frequency fluctuations?" *IEEE Trans. Ultrason. Ferroelect., Freq. Contr.,* vol. 36, pp. 452–458, Mar. 1989.

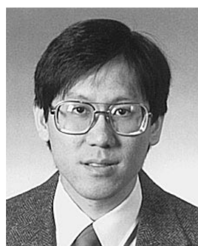

Clark T.-C. Nguyen (S'90–M'95) was born in Austin, TX, on March 29, 1967. He received the B.S., M.S., and Ph.D. degrees from the University of California at Berkeley in 1989, 1991, and 1994, respectively, all in electrical engineering and computer sciences.

In 1995, he joined the Faculty of the University of Michigan, Ann Arbor, where he is currently an Assistant Professor in the Department of Electrical Engineering and Computer Science. His research interests focus upon microelectromechanical systems and include integrated micromechanical signal processors and sensors, merged circuit/micromechanical technologies, RF communication architectures, and integrated circuit design and technology. From 1995 to 1996, he was a Member of NASA's New Millennium Integrated Product Development Team (IPDT) on communications and is presently a Consulting Member.

Roger T. Howe (S'80–M'80–SM'93–F'96) received the B.S. degree in physics from Harvey Mudd College, Claremont, CA, in 1979 and the M.S. and Ph.D. degrees from the University of California, Berkeley, in 1981 and 1984, respectively, both in electrical engineering.

He is a Professor of electrical engineering and computer science and of mechanical engineering, as well as a Director of the Berkeley Sensor & Actuator Center. His research program has concentrated on polysilicon integrated microsystems technology over the past decade. He and his students have made contributions to the electrostatic actuation of microresonators (the interdigitated comb drive), merge CMOS/polysilicon microstructure processes, and a closed-loop digital control of suspended microstructures.

Dr. Howe was General Chairman of the 1996 Solid-State Sensor and Actuator Workshop at Hilton Head, SC, and was a Cogeneral Chairman of the 1990 IEEE/ASME MEMS Workshop. He was a corecipient (with R. S. Muller) of the 1998 IEEE Cledo Brunetti Award for pioneering contributions to MEMS.